Purdue University

Purdue e-Pubs

CTRC Research Publications   Cooling Technologies Research Center

2011

Characterization of the Heat Transfer Accompanying Electrowetting-Induced Droplet Motion

Niru Kumari
Purdue University

S V. Garimella
Purdue University, sureshg@purdue.edu

Follow this and additional works at: http://docs.lib.purdue.edu/coolingpubs

Characterization of the heat transfer accompanying electrowetting or gravity-induced droplet motion

Niru Kumari and Suresh V. Garimella[*]
Cooling Technologies Research Center, an NSF I/UCRC
School of Mechanical Engineering and Birck Nanotechnology Center
Purdue University, West Lafayette, IN 47907

ABSTRACT

Electrowetting (EW) involves the actuation of liquid droplets using electric fields and has been demonstrated as a powerful tool for initiating and controlling droplet-based microfluidic operations such as droplet transport, generation, splitting, merging and mixing. The heat transfer resulting from EW-induced droplet actuation has, however, remained largely unexplored owing to several challenges underlying even simple thermal analyses and experiments. In the present work, the heat dissipation capacity of actuated droplets is quantified through detailed modeling and experimental efforts. The modeling involves three-dimensional transient numerical simulations of a droplet moving under the action of gravity or EW on a single heated plate and between two parallel plates. Temperature profiles and heat transfer coefficients associated with the droplet motion are determined. The influence of droplet velocity and geometry on the heat transfer coefficients is parametrically analyzed. Convection patterns in the fluid are found to strongly influence thermal transport and the heat dissipation capacity of droplet-based systems. The numerical model is validated against experimental measurements of the heat dissipation capacity of a droplet sliding on an inclined hot surface. Infrared thermography is employed to measure the transient temperature distribution on the surface during droplet motion. The results provide the first in-depth analysis of the heat dissipation capacity of electrowetting-based cooling systems and form the basis for the design of novel microelectronics cooling and other heat transfer applications.

Keywords: Heat transfer, droplet motion, electrowetting

---

[*] Corresponding author: sureshg@purdue.edu, (765) 494 5621

NOMENCLATURE

c_p	specific heat capacity, $J/(kg\text{-}K)$		F	force, N
h	heat transfer coefficient, $W/(m^2\text{-}K)$		H	plate spacing, m
k	thermal conductivity, $W/(m\text{-}K)$		R	droplet radius, m
P	pressure, Pa		T	temperature, $°C$
q''	heat flux, W/m^2		V	velocity, m/s

q'' — heat flux, W/m^2 V — velocity, m/s

$\dot{q}'''$ volumetric heat source, W/m^3

Greek

t time, s

α thermal diffusivity, $m^2\text{-}s$

$\vec{v}$ velocity vector, m/s

μ dynamic viscosity, $Pa\text{-}s$

x distance along direction of droplet motion (in the plane of the heated surface), m

ρ mass density, kg/m^3

Subscripts

a ambient

y distance normal to droplet motion (in the plane of the heated surface), m

d droplet

s surface

z distance along droplet height, m

INTRODUCTION

The field of electrowetting [1,2] has received significant attention over the past decade because of enhanced microfluidic control options, low power consumption and amenability to integration with microelectronics packaging. The key application areas driving this interest include lab-on-chip systems, electrowetting-based optics and liquid displays. There has been recent interest in using electrowetting for heat transfer applications [3-5]; as an illustration, electrowetting-based microelectronics thermal management (package level as well as site-specific hot spot thermal management) has been the focus of some recent research efforts.

While there have been a number of studies in the literature on the heat transfer characteristics of other types of droplet-based systems such as sprays [6-12] and mist [13, 14], the thermal characteristics associated with the motion of discrete liquid droplets have not been well mapped and understood. The heat dissipation capacity associated with a stationary evaporating droplet on a surface has been studied in detail for fire suppression applications [15, 16]. The heat transfer from a hot steel surface to stationary water droplets (diameter ~ 2 *mm*) with various contact angles (90°, 55° and 20°) was experimentally measured and modeled by Chandra *et al.* [15]. The focus of that work was to study the dependence of the droplet evaporation rate on the contact angle. The contact angle was varied in the experiments by the

addition of surfactants to the liquid. Fukai *et al.* [17] performed experiments which involved droplets sliding on a hot inclined substrate; however, the focus of the work was to study the effect of the heat flux on the dynamic contact angle of the droplet. Another study of stationary droplet-based transient cooling of a hot substrate was conducted by Tarozzi *et al.* [18]. An infrared transparent substrate (BaF$_2$) and infrared thermography were employed to thermally map the contact area of the substrate and the cold droplet.

Unlike the focus of the studies discussed above, electrowetting-based cooling schemes do not typically rely on evaporative cooling. Only a few studies have reported experimental measurements of the heat transfer performance of electrowetting-based droplet systems. Pamula and Chakrabarty [3] suggested the use of an electrowetting-based digital microfluidic system for cooling hot spots in integrated circuits. They also proposed a dynamic cooling system utilizing thermocapillarity and electrowetting; hot spots on the chip would attract higher flow rates due to thermocapillarity, and this hot fluid would be returned to the reservoir using electrowetting-based pumping. Paik *et al.* [19] experimentally investigated the effect of temperature on droplet velocities by evaluating the temperature-dependence of filler fluid viscosity and filler fluid-droplet surface tension. Oprins *et al.* [20] and Mohseni [5] carried out simplified experiments to study droplet flows in microchannels, but did not obtain temperature measurements. Paik *et al.* [4] demonstrated via measured temperature decreases that EW can be used for hot-spot cooling.

Modeling of EW-actuated droplet heat transfer has received less attention. Preliminary feasibility calculations by Pamula and Chakrabarty [3] showed that up to 90 *W/cm^2* of heat dissipation is possible from an array of droplets flowing on a chip without any area enhancement. Oprins *et al.* [21] modeled the internal flow and heat transfer inside a two-dimensional droplet moving between two plates under electrowetting actuation. The heat transfer was found to be enhanced by a factor of 2 compared to the case of a static droplet with conduction as the only heat transfer mode. Baird and Mohseni [22] solved the two-dimensional flow and energy equations to predict the heat transfer associated with droplet movement between two heated, isothermal plates; three-dimensional effects of liquid flow circulation were not considered. Bahadur and Garimella [23, 24] introduced the concept of an electrically tunable thermal resistance switch which relies on the use of an electrowetting voltage to switch between the nonwetting (high thermal resistance to heat transfer) and wetting (low thermal resistance) states of superhydrophobic surfaces. It is noted that numerical analysis of the heat transfer associated with EW-induced droplet motion is complicated by the coupling of the momentum and energy equations through the temperature-dependent viscosity and surface tension.

The present work undertakes a fundamental investigation of the heat transfer accompanying EW-induced droplet motion on a single plate and between two parallel plates. Precise temperature measurements are obtained to experimentally estimate the cooling capacity of a droplet as it slides down an inclined heated surface. A numerical model is developed to further understand and quantify the heat transfer; results from the model are benchmarked against the experimental measurements. The numerical model is then utilized to predict the heat dissipation performance of droplets moving between two parallel plates, which is a common microfluidic configuration. Finally, the cooling performance of discrete droplet-based pumping is compared to that obtained with continuous flows.

EXPERIMENTAL CHARACTERIZATION OF HEAT TRANSFER TO A MOVING DROPLET

Figure 1 (a) shows a schematic diagram of the experimental setup designed for measuring the heat dissipation capacity of a droplet sliding down an inclined plate. The plate is attached to a tilt stage that can adjust plate inclination to the desired angle. Electrowetting is not employed to actuate the droplets in the experiments; instead, droplets move under the influence of gravity at velocities commonly encountered in electrowetting actuation. The plate is made of glass and has dimensions of 15 *cm* × 15 *cm* × 0.5 *mm*. A part of the bottom side of the plate (12 *cm* × 15 *cm*) is coated with an Indium Tin Oxide (ITO) layer, as shown in cross section in Figure 1(b). A DC power supply is utilized to resistively heat the ITO layer such that it dissipates a constant heat flux of 2000 W/m^2 over the heated section (estimated from the measured current and voltage difference across the ITO layer, and the surface area of the ITO layer). The upstream section of the plate is left uncoated and unheated; the length of this non-heated section is chosen such that the droplet (which is deposited well upstream of the heated section) reaches its terminal velocity before encountering the heated portion of the plate. Electrical connections to the ITO layer are made using electrically conductive silver epoxy. A thin layer of black paint (Krylon # 1602 with known thermal emissivity of 0.95 [25]) is sprayed on the lower surface of the plate; the temperature of the lower surface can be estimated using an infrared camera. The upper surface of the plate is spin-coated with a thin (50 *nm*) layer of Teflon to render it hydrophobic.

The experiments consist of depositing a droplet of a known volume and initial temperature (22 ^oC) on the unheated part of the plate and recording the droplet velocity and temperature profile along the plate. The plate is held at tilt angles ranging from 30° to 60°, which determines the droplet velocity as it slides under the influence of gravity. Droplet motion is recorded using a high-speed camera (Pixelink) positioned above the plate as shown in Figure 1(a); the high-speed image sequences are used to estimate droplet velocity. The heat dissipation capacity of the droplet is quantified by measuring the reduction in wall temperature using an infrared camera (ThermaCAM Merlin) at 60 fps with a resolution of 0.375 *mm*

4

$\times$ 0.375 *mm*. The infrared camera was calibrated using a highly-sensitivity blackbody (2000 series, SBIR Inc.).

Ethylene glycol (EG) and water are the two fluids utilized in this work. The low vapor pressure of ethylene glycol ensures negligible evaporative cooling, so that the temperature reduction achieved can be directly attributed to heat conduction and convection. The experiments with water droplets have an evaporative cooling component; however, the contribution of evaporative cooling can be accounted for by comparing the experimental results against a validated numerical model, as described in the next section.

Table 1 summarizes the volumes of all the droplets considered in the experiments and the measured velocities obtained with these droplets at different tilt angles. Droplet velocity is estimated by plotting the position of the center of the droplet versus time; as an illustration, Figure 2(a) shows the time-varying position of a 5 μl EG droplet. It is seen that the droplet position can be approximated as a linear function of time, indicating that the droplet velocity is constant, and it has reached its terminal velocity. The uncertainty in measurement of the droplet velocity is estimated to be approximately ±0.1 *cm/s*. Table 1 shows that the droplet velocities increase with tilt angle as expected. The velocities for water droplets are higher than for ethylene glycol droplets due to the smaller viscosity and higher surface tension of water; these properties influence the advancing and receding contact angles which in turn determine the driving force for the sliding motion [26]. Experiments for each case listed in Table 1 were repeated 3 times. The experimental results varied within the experimental uncertainty limits for each case; the experimental results are presented from a representative test run for each case.

Figure 2(b) shows a representative infrared temperature map for the case of a 5 μl EG droplet moving at 3.95 *cm/s*. It should be noted that the infrared camera measures the temperatures at the lower surface of the heated plate (and the temperature of the upper surface is estimated using numerical modeling as will be discussed). The heated section of the plate shows a constant temperature of approximately 72 ^{o}C; the upstream, unheated section also increases in temperature due to conduction through the plate. The temperature drop associated with the motion of a cold droplet can be seen along the droplet path. Such temperature maps are utilized in the present work to quantify the cooling capacity of the droplet. In part due to the careful calibration of the IR camera, the uncertainty in measurement of the wall temperature is approximately ± 0.2 °C.

Figure 3 (a)-(c) show the transient temperature decreases (along the droplet centerline trajectory) resulting from heat transfer to a 5 μl EG droplet moving at three different velocities. The temperature decreases are only plotted over the heated section of the substrate, i.e., $x > 3$ *cm*. From the plots, the maximum temperature decreases are measured to be approximately 3.8 ^{o}C, 3 ^{o}C and 1.8 ^{o}C for $V = 2.85$, 3.95 and 9 *cm/s*, respectively. The droplet heats up as it moves downstream; this reduces its heat removal

capacity which results in less cooling in the downstream regions of the heated section. Also, the plate temperature at any location is seen to increase after the droplet has moved away from that location. Interestingly, it is seen that at the low velocities of $V = 2.85$ *cm/s* and $V = 3.95$ *cm/s*, the droplet has a cooling effect downstream of its position. As an illustration, Figure 3(a) shows that a section up to x = 3.4 *cm* experiences a cooling effect at $t = 0.1$ *s*, even though the droplet center is at $x = 3.07$ *cm* (the droplet footprint is between x = 2.93 and 3.21 *cm*). However, according to Figure 3(c), the droplet with a higher velocity of 9 *cm/s* does not result in a temperature reduction downstream. This phenomenon of downstream cooling is directly related to the thermal diffusivity of the plate and the residence time of the droplet on the plate (which depends on its velocity).

Smaller temperature decreases are observed on the lower surface with faster-moving droplets. This may appear to be counter-intuitive as the convective heat transfer coefficient would increase with an increase in droplet velocity. This seemingly anomalous result is attributed to the temperature measurements being obtained on the lower surface while the droplet slides along the upper surface; the associated thermal mass of the glass plate is the primary contributor to this anomaly. It will be shown in the next section that the temperature decrease on the upper surface is indeed higher for faster-moving droplets. Another interesting observation from Figure 3(a)-(c) is that the transient temperature profiles for $V = 2.85$ *cm/s* show different shapes as compared to those obtained at higher velocities. For the case of $V = 3.95$ and 9 *cm/s*, the temperature drops decrease consistently with time; for the case of $V= 2.85$ *cm/s*, however, the temperature drop shows a peak around $x = 4.7$ *cm* at $t = 0.8$ *s* (droplet center at 4.84 *cm*). The reason for this behavior is the recirculating flow field inside the droplet which will be discussed in the next section.

Transient lower-surface temperature decreases (along the droplet centerline trajectory) with a larger, 6.5 *μl* EG droplet (not shown) were similar to the trends seen in Figure 3(a)-(c). The maximum temperature decreases on the lower surface temperature were approximately 3.2, 2.4 and 1.8 ^oC for velocities of 4.66, 6.36 and 10.71 *cm/s*, respectively. The droplet at the lowest velocity of 4.66 *cm/s* showed a cooling effect downstream of its location; this effect was not seen in the other two cases. A comparison of results for the two droplet volumes showed that the maximum temperature decrease does not show a strong dependence on droplet size. However, a direct comparison between the two cases is not appropriate as the droplet velocities are also different; the bigger droplet also cools a larger surface area.

Additional heat transfer experiments were carried out with deionized water droplets to estimate the influence of liquid thermal properties on heat dissipation. Figure 4(a) shows transient temperature decreases for a 5 *μl* water droplet moving at 9 *cm/s*, while Figure 4(b) is for a 6.5 *μl* water droplet moving

at 12.6 *cm/s*. The temperature reduction trends are similar to those obtained with EG droplets. The maximum temperature reduction obtained is 5.1 and 4.4 $^o C$ for the two cases, respectively. A comparison of the results in Figure 3(c) and Figure 4(a) also illustrate the greater cooling obtained with water droplets due to its higher heat capacity compared to EG.

NUMERICAL MODELING OF HEAT TRANSFER TO A MOVING DROPLET

Since experimental measurement of temperatures on the upper surface of a plate along which a droplet moves is challenging, one approach to quantifying the cooling achieved with droplets is to measure the effect on the lower surface of the wall and estimate the corresponding reduction in temperature along the upper surface by numerical modeling. A better understanding of the heat dissipation associated with a moving droplet is also achieved with such a model, and is one of the major objectives underlying the present work. The validated model is then extended to study the heat transfer associated with a droplet moving between two plates, which is a common configuration encountered in microfluidic applications.

The present study utilizes a finite volume approach using the commercially available software package FLUENT [27] to model the droplet motion in two configurations. The modeling involves a solution of the following coupled mass, momentum and energy equations in the droplet and the hot plate:

$$\frac{\partial \rho}{\partial t} + \nabla(\rho \vec{v}) = 0 \tag{1}$$

$$\frac{\partial}{\partial t}(\rho \vec{v}) + \nabla(\rho \vec{v} \cdot \vec{v}) = -\nabla P + \mu(\nabla \cdot \nabla \vec{v}) + \rho \vec{g} \tag{2}$$

$$\frac{\partial}{\partial t}(\rho c_P T) + \nabla(\rho \vec{v} c_P T) = \nabla \cdot (k \nabla T) + \dot{q}''' \tag{3}$$

where ρ is the material density, $\vec{v}$ is the velocity vector, μ is the material-specific dynamic viscosity, $\vec{g}$ is the gravitational force, T is the temperature, c_p and k are material-specific heat and thermal conductivity, respectively, and $\dot{q}'''$ is the volumetric heat generation rate. The material properties for ethylene glycol are: ρ = 1115 *kg/m³*, μ = 0.014 *Pa-s*, c_p = 2200 *J/(kg-K)* and k = 0.24 *W/(m-K)*; for water: ρ = 998 kg/m³, μ = 0.00089 *Pa-s*, c_p = 4180 *J/(kg-K)* and k = 0.6 *W/(m-K)*; for glass: ρ = 2520 kg/m³, c_p = 1020 *J/(kg-K)* and k = 0.6 *W/(m-K)*; and for silicon: ρ = 2330 kg/m³, c_p = 712 *J/(kg-K)* and k = 148 *W/(m-K)*.

1. SINGLE-PLATE CONFIGURATION

Figure 5(a) shows the computational domain for the study of the heat transfer associated with a droplet moving on a heated plate. The computational domain for the droplet motion between two plates is also shown (Figure 5(b)) and will be discussed in the next section. In Figure 5(a), the glass plate is 15 *cm* × 15 *cm* × 0.5 *mm* in dimension just as in the experiments. The indium tin oxide layer is modeled as a 1 *μm* thick heat-generating layer. The side walls of the plate are adiabatic and a convective heat transfer condition of (h_a, T_a) of (20 *W/m²K*, 22 *°C*) is applied on the upper and lower surfaces of the plate to match the steady-state plate temperature in the experiments with no droplet motion. The droplet is modeled as a hemispherical cap with a radius of 1.37 *mm* or 1.48 *mm* representing the 5 *μL* and 6.5 *μL* droplet, respectively. The contact angle of the droplet is fixed to be 90° and the change in droplet shape due to motion is ignored. These assumptions are justified as the velocity field obtained in the present work is similar to that obtained from a detailed model of the droplet shape employing different advancing and receding angles [28]. The velocity field in the droplet moving between two plates (with similar assumptions) also matches the velocity field obtained with a more detailed model considering the droplet shape [21]. The droplet-air interface is modeled as a no-shear boundary condition, with an applied convective heat transfer condition. The frame of reference is fixed to the droplet, and a constant velocity *V* is applied to the plate in the negative *x*-direction.

A mesh-independence study was carried out to determine the grid sizes needed for the numerical simulations. The heat transfer coefficient between the droplet and the surface (defined later) changed by approximately 10% when the number of grid cells was increased from 320,000 to 880,000, and only by less than 1% for a further change from 880,000 to 1,600,000. All the simulations presented in this paper were thus carried out using 880,000 cells. The time step was selected as 0.001 *s*; it was verified that the results changed by less than 0.2% when the time step was decreased from 0.001 *s* to 0.0005 *s*.

The numerical model was benchmarked by comparing predictions against the experimental heat transfer measurements. The predicted transient temperature profile on the lower surface of the plate is compared with the measured profile. As shown in Figure 6(a)-(b) for the case of an ethylene glycol droplet sliding on an inclined heated plate at velocities of 3.95 and 9 *cm/s*. Figure 6(c) shows a similar comparison for the case of a water droplet sliding at a velocity of 9 *cm/s*. The droplet is at its terminal velocity in all the comparisons. The *x'* in Figure 6 represents the axial distance (in the flow direction) measured from the point where the droplet reaches its terminal velocity; in the model, this is the point after which the velocity field inside the droplet reaches a fully developed condition. The comparison is shown over an axial distance of 1.2 *cm* about the droplet center (approximately 6 radii upstream and downstream of the droplet center). It is seen that the predicted and measured temperature profiles show reasonable agreement within the limits of experimental uncertainty for all the three cases. This

comparison validates the assumptions in the present model, especially with respect to the use of a single heat transfer coefficient all around the droplet, the hemispherical shape of the droplet, and the use of identical advancing and receding contact angles for the droplet. The good match between experiments and simulations for the water droplet also indicates that evaporative cooling is not significant as compared to convective cooling; this is explained by the small residence time of the droplet on the hot plate.

A snapshot of the velocity vectors inside a 5 μL ethylene glycol droplet moving at a droplet velocity of 3.95 cm/s are shown in Figure 7; several different cross-sectional planes are shown to reveal the complex nature of the flow field at a single instant in time, $t = 0.1$ s. For this case, the flow was found to reach a fully developed state by $t = 0.045$ s (when the droplet center was at x = 1.78 mm). Velocity vectors in xz planes are shown in Figure 7 (a)-(b) at $y = 0$ and $y = 0.4$ mm. A circulating flow pattern is seen inside the droplet; liquid flows in the positive x direction close to the plate (small z) and in the negative x direction higher up (large z). The center of the vortex is seen to shift from $(x, z) = (3.8, 0.4)$ mm at the $y = 0$ mm center plane to $(x, z) = (4.2, 0.5)$ mm at the $y = 0.4$ mm showing the three-dimensional nature of the flow. The flow patterns can be analyzed in more detail by considering various z planes at this time instant as shown in Figure 7(c)-(h). Close to the plate, at $z = 0.05$ mm, the flow is predominantly in the negative x direction due to no-slip at the wall as seen in Figure 7(c). At $z = 0.2$ mm, the flow points upward (positive z) near the leading edge of the droplet and downward near the trailing edge; in the central region of the droplet, the flow continues to be mostly in the negative x-direction (Figure 7 (d)). A similar flow pattern is seen at $z = 0.4$ mm with vertical flow over much of this plane (Figure 7(e)). By $z = 0.5$ mm, vertical flow is seen in the entire plane; the flow direction in the two halves is opposite which results in two vortices at $x = 4$ mm and $y = \pm 0.8$ mm, as shown in Figure 7(f). The vortices move out to the droplet-air interface ($y = \pm 1.1$ mm) at z = 0.6 mm (Figure 7(g)). The flow direction is reversed to the positive x direction for $z > 0.6$ mm as shown in Figure 7(h).

Figure 8(a) shows the average heat flux q_s'', the average surface temperature T_s at the droplet-plate interface, and the volume-averaged droplet temperature T_d as a function of the position of the droplet center, x_d. Figure 8(b) shows details of the variation of q_s'' and T_s in the region $0 < x_d < 1$ cm. The mean droplet temperature increases monotonically with distance as expected; however q_s'' and T_s do not show a monotonic dependence on x_d. The shapes of these profiles can be understood by studying the temperature distribution in different xz planes and at the droplet-plate interface (Figure 9(a)), as well as along the droplet-air interface (Figure 9(b)). The six time instants at which the plots in Figure 9 are shown are marked in Figure 8(b). The heat flux is very high as soon as the droplet encounters the heated region as shown in Figure 8 because of the high temperature difference available between the plate and droplet.

The maximum temperature decrease on the upper surface of the heated plate is approximately 15 ^oC at the beginning of the heated section (from 72 ^oC to 57 ^oC). A thermal boundary layer is seen to develop in the droplet due to heating from the plate from (t, x_d) of (0.005 s, 0.2 mm) to (0.045 s, 1.8 mm) shown as panels (i) – (iii) in Figure 9. As this thermal boundary layer grows, q_s'' decreases while T_s increases. While the thermal boundary layer thickness remains constant between points (iii) and (v), cold liquid is drawn to the plate by recirculation and results in q_s'' and T_s being constant till (t, x_d) = (0.125 s, 5 mm) as shown in Figure 8(b). Eventually, as the hot liquid in the droplet reaches the leading edge of the droplet by recirculation, the cooling capacity is reduced; this is seen as a decrease in q_s'' and an increase in T_s (from point (vi) forward in Figure 8(b) and Figure 9). The temperature distribution along the droplet-air interface in Figure 9(b) shows trends consistent with this explanation. This cycle of variation of q_s'' and T_s repeats every 6.9 mm (0.17 s) which is the circulation distance of the liquid inside the droplet, i.e., the length along the droplet and circumference of the droplet-air interface. The phenomenon subsides once the droplet has reached thermally developed conditions. Similar oscillatory behavior of the heat transfer coefficient was also reported by Baird and Mohseni [22].

The temperature profiles obtained above can be used to estimate the heat transfer coefficient h which is defined as:

$$h = \frac{q_s''}{T_S - T_d} \tag{4}$$

where, q_s'' is the surface heat flux, T_s is the average temperature of the surface over the droplet footprint, and T_d is the mean droplet temperature. A Nusselt number Nu can also be estimated using a length scale which is the ratio of the droplet volume to the droplet-plate contact area, i.e., $\frac{2R}{3}$. Figure 10(a) plots the heat transfer coefficient h and Nusselt number Nu as a function of the droplet position x_d for a 5 μL ethylene glycol droplet moving at three different velocities. The oscillations in the curves result from the liquid circulation effects discussed above. The time period for these oscillations depends on the droplet velocity. The initial values of the heat transfer coefficient and the Nusselt number are approximately the same for all three droplet velocities. The steady-state value of (h, Nu) are (2140 W/m^2K, 7.57), (2239 W/m^2K, 7.91) and (3076 W/m^2K, 10.66) for droplet velocities of 2.85, 3.95 and 9 cm/s, respectively. The corresponding values for a larger 6.5 μL ethylene glycol droplet as shown in Figure 10(b) are (2196 W/m^2K, 8.47), (2434 W/m^2K, 9.41) and (3239 W/m^2K, 12.5) for droplet velocities of 4.66, 6.36 and 10.7 cm/s, respectively.

Similar results for water droplets are summarized in Figure 11 for a 5 μL water droplet moving at 9 cm/s and a 6.5 μL droplet moving at 12.6 cm/s; Figure 11(b) shows the corresponding h. The smaller droplet with the lower velocity results in a lower heat flux as compared to the faster, larger droplet. The smaller droplet also heats up faster. However, the wall temperatures for the two droplets are quite comparable. The heat transfer coefficients shown in Figure 11(b) exhibit similar trends as those for ethylene glycol droplets. Figure 11(b) does not show Nu since the characteristic length scale is different for the two droplets. Steady-state values of (h, Nu) are obtained as (7529 W/m^2K, 11.2) and (7347 W/m^2K, 12) for the 5 μL and 6.5 μL water droplets, respectively. The heat fluxes and heat transfer coefficients are higher for the water droplets compared to the EG droplets due to the higher specific heat capacity of water. As an illustration, the heat transfer coefficient resulting from the movement of a 5 μL water droplet at 9 cm/s is approximately three times higher than that obtained from a similarly sized ethylene glycol droplet moving at the same velocity. The initial wall temperature decrease for water droplets of approximately 22 $°C$ is higher than the 15 $°C$ observed with EG droplets

2. TWO-PLATE CONFIGURATION

Heat transfer due to the motion of droplets sandwiched between two parallel plates is considered here, as this is a common configuration encountered in droplet actuation and microfluidic systems. The modeling framework developed and validated for the one plate model is utilized here to predict the heat dissipation capacities of droplets moving between two plates.

In the computational domain shown in Figure 5(b) the bottom plate is selected as silicon (k = 148 W/mK, α = 8.8 × 10^{-5} m^2/s) which is a common choice of material in many studies. The bottom plate has dimensions of 15 cm × 15 cm × 0.3 mm with a 1 μm layer on the bottom surface set as a heat-generating source. The side walls of the plate are adiabatic and a convective heat transfer condition of (h_a, T_a) of (86 W/m^2K, 22 $°C$) is applied on the upper and lower surfaces of the silicon plate to maintain a steady-state temperature of 80 $°C$ with no droplet motion. The top wall as well as the droplet-air interface are modeled as adiabatic; the adiabatic condition on the droplet-air interface ensures that the droplet is not cooled by the ambient air, to mimic the case of a droplet-based heat sink. Water is selected as the fluid and the droplet is modeled as a cylinder with radius R; the change in shape due to droplet movement is neglected. The droplet-air interface is modeled as a no-shear boundary condition. The frame of reference is fixed to the droplet, and a constant velocity V in the negative x-direction is applied to the top and bottom plates.

Parametric studies are carried out to estimate the influence of droplet size, droplet velocity and plate spacing on heat transfer. The first set of simulations consider 5 μL (R = 1.78 mm) water droplets moving

between two plates with a spacing of $H = 0.5$ *mm* at velocities of 5, 7.5 and 10 *cm/s*; this set of simulations quantifies the influence of droplet velocity on heat transfer. Additional simulations are carried out with droplet velocities fixed at 10 *cm/s* with (droplet volume, radius, plate spacing) combinations of $(1\mu L, R = 0.79$ *mm*, $H = 0.5$ *mm*) and $(1\mu L, R = 1.78$ *mm*, $H = 0.1$ *mm*).

Figure 12 shows the velocity vectors (colored by the velocity magnitude) and the velocity profiles obtained from the motion of a 5 μL water droplet moving at 10 *cm/s* between two plates with a spacing of 0.5 *mm*. These plots correspond to a time of 0.1 *s* after the droplet starts moving (droplet center at $x = 10$ *mm*). Figure 12(a) – (b) show the velocity vectors in the *xz* plane at $y = 0$ at the leading and trailing edges of the droplet, respectively. The flow is seen to have two recirculation regions which are symmetric about the midplane $z = 0.25$ *mm*. Details of the flow field on *xy* planes are shown in Figure 12(c) – (e) for $z = 0$ *mm*, 0.1 *mm* and 0.2 *mm*, respectively (the flow profiles are similar at $z = 0.5$, 0.4 and 0.3 *mm* and are not shown). It is seen that the flow is in the negative *x* direction in the region close to the plates ($z <$ 0. 1 *mm* and $z > 0.4$ *mm*) and in the positive *x* direction for 0.2 *mm* < z < 0.3 *mm*. Two vortices are seen at $z = 0.1$ *mm* with centers at $x = 8.8$ *mm* and $y = \pm 0.8$ *mm*. These results capture the complex three-dimensional nature of the flow fields. The velocity profiles v_x and v_z on the $y = 0$ *mm* plane at different axial locations are shown in Figure 12(f). The velocity has a parabolic profile over most of the axial distance, except in regions close to the leading and trailing edges of the droplet. It is interesting to note that v_x is smaller at *x* coordinates upstream of the droplet center and larger at *x* coordinates downstream of the droplet center. This is because of the development of the velocity boundary layer along the droplet length. The magnitude of velocity component v_z is negligible across most the droplet, except towards the trailing and leading edges of the droplet.

Temperature contours at seven *xz* planes in the droplet are shown in Figure 13(a) at $t = 0.1$ *s* (droplet center is at $x = 10$ *mm*); the interface temperature contour between the droplet and the bottom plate is also indicated in this plot. Figure 13(b) shows the temperature profiles at different axial locations at $y = 0$. The thermal boundary layer is seen to be grown along the *x*-direction. Figure 13(b) also shows a very high temperature gradient at the leading edge of the droplet as compared to the trailing edge. At the leading edge ($x_{rel} = 1.75$ *mm*; $x = 11.75$ *mm*), the temperature in the droplet changes sharply from 74 °*C* at the surface to 36 °*C* at $z = 0.02$ *mm*; at the trailing edge ($x_{rel} = -1.75$ *mm*; $x = 11.75$ *mm*), on the other hand, the same temperature decrease from 74 °*C* to 36 °*C* occurs at $z = 0.25$ *mm*; this results in a much lower temperature gradient at the trailing edge as compared to the leading edge. Also, it is seen that the top half of the droplet ($z > 0.25$ *mm*) is at significantly lower temperatures than the bottom half. This is because of the lack of flow mixing across the mid *z* plane ($z = 0.25$ *mm*) resulting from the velocity profile shown in Figure 12. Heat transfer across the two halves of the droplet is therefore dominated by

heat diffusion. The characteristic time for diffusion is approximately $H^2/\alpha = 1.74$ s; this is much higher than the time period of the simulation (0.1 s). The results of these simulations highlight the importance of conducting careful analyses of the flow patterns; many of the present results are non-intuitive and significantly impact thermal transport in the droplet.

Figure 14 shows the heat transfer coefficient h and Nusselt number Nu for a 5 μL water droplet moving at three different velocities; it is seen that all three cases have the same trend of variation with droplet position. The h and Nu start of being very high and then attain a constant value after an axial distance of about 0.1 mm. The heat transfer coefficient and the Nusselt number increase with droplet velocity. The (h, Nu) values obtained at the downstream end of the simulation domain are (5895 W/m^2K, 4.91), (7016 W/m^2K, 5.9) and (10637 W/m^2K, 8.9) for droplet velocities of 5, 7.5 and 10 cm/s respectively. The important difference from the single-plate heat transfer results is the lack of an oscillatory behavior in the profiles of h and Nu in this case. This is because the recirculation length is twice the droplet diameter and the plate spacing of 7.64 mm which is close to the length scale studied in the simulation.

As for the single-plate configuration, Figure 15(a) compares q_s'', T_s and T_d for three water droplets with (volume, radius R, plate spacing H) corresponding to (5 μL, 1.78 mm, 0.5 mm), (1 μL, 0.79 mm, 0.5 mm) and (1 μL, 1.78 mm, 0.1 mm) moving at a velocity of 10 cm/s. Figure 15(b) shows the corresponding h and Nu for the three cases. The second case has the highest heat flux, followed by the first case. The heat transfer coefficient is highest for the third case followed by the second case. The third case has the highest rate of droplet temperature rise because of its high area to volume ratio. For this case, the difference between the surface temperature and the droplet temperature is very small for $x_d > 0.4$ cm; this results in a high value of h (from the definition of the heat transfer coefficient). It can be concluded from Figure 15 that the heat transfer coefficients are higher for small droplet volumes and lower plate spacings. Analyses such as this are necessary to arrive at an optimum geometry which maximizes the heat transfer coefficient or wall temperature reduction for a given problem.

HEAT DISSIPATION CAPACITY OF ELECTROWETTING-BASED SYSTEMS

The dependence of heat transfer coefficients on droplet velocity, actuation geometry and fluid properties was elucidated above. These results are now used to estimate the heat dissipation capacity of a system of droplets moving under electrowetting actuation, to provide an estimate of the thermal performance in practical applications. In the example considered, droplets flow in discrete rows on a hot surface with an area of 12 mm × 12 mm. The lateral and longitudinal spacing between neighboring droplets in the array is assumed to be 0.1 mm; this distance also depends on packaging constraints and should be sufficiently large to avoid droplet merging. The maximum surface temperature is assumed to

be 80 °C. The average heat transfer coefficient associated with a single droplet is obtained from the simulations in the previous section. The average heat flux removal capacity of a single droplet is estimated by multiplying the average heat transfer coefficient and the temperature difference between the surface and the inlet liquid. The overall heat dissipation capacity of this system of droplets is estimated by multiplying the heat flux dissipation capacity of a single droplet with the fraction of the area of the surface covered by the droplets. Table 2 compares the heat dissipation results for the three different kinds of droplets shown in Figure 15. It is clear from the table that a system consisting of 1 μL water droplets with a plate spacing of 0.5 mm can support a heat dissipation rate of approximately 59 W under a single droplet, and an average heat dissipation rate over the entire plate area of 40 W/cm^2.

The performance of electrowetting-based cooling systems is now compared with that of continuous flow systems such as a flow through a microchannel. Microchannel-based heat sink cooling utilizing single-phase flow is well studied and characterized [29]. The comparison between these two competing technologies is carried out under the constraint of the same pumping power for flow in the heat sink (having a footprint area of 12 × 12 mm^2). The pumping power required for the external loop is not considered in the calculations and is usually much lower than the power required to sustain flow in the heat sink. The second droplet-based case in Table 2 is selected for comparison. The pumping power for electrowetting-based actuation can be estimated by calculating the power required to charge the capacitive layer underneath the droplets. The electrowetting actuation force depends on a gradient of the capacitive energy underneath the droplet; this capacitance exists in the form of a dielectric layer on top of the actuation electrodes. The power required for electrowetting-based actuation can be estimated using:

$$\dot{W}_{EW} = \frac{0.5CV^2 \, n_d}{\Delta t} \tag{5}$$

where V is applied voltage (approximately 50 V [30]), n_d is the number of droplets on the heat sink (49 from Table 2), and C is the capacitance associated with a droplet which is defined as:

$$C = \frac{\varepsilon_r \varepsilon_o A_d}{t_{diel}} \tag{6}$$

In the above equation, ε_o is the dielectric constant of vacuum which is 8.85 x 10^{-12} F/m, ε_r is the dielectric constant of the dielectric layer (for Parylene C dielectric layer, $\varepsilon_r = 3$), A_d is the base area of the droplet, and t_{diel} is the thickness of the dielectric layer (1 μm). The time interval Δt is the time require by a droplet to move a length equal to its diameter and depends on the droplet velocity as follows:

$$\Delta t = \frac{2R}{V} = 1.6 \times 10^{-2} s \tag{7}$$

Using the equations described above, the pumping power required to drive the electrowetting-based heat sink (actuation of 1 μL water droplets at 10 cm/s between two plates with spacing 0.5 mm) is estimated as $\dot{W}_{EW} = 0.2\ mW$.

Two kinds of microchannel-based heat sinks are included in the comparison. The first involves a single channel with slug flow (channel width of 12 mm), while the second heat sink consists of 40 microchannels (channel width of 0.2 mm). The channel height in both these cases is the same as that in the electrowetting-based heat sink (0.5 mm). The flow velocity in the microchannels is estimated such that the pumping power consumed by the microchannel is 0.2 mW. The pumping power to sustain single-phase laminar flow is estimated using the following equation:

$$\dot{W}_{MC} = dP \times \dot{Q} \tag{8}$$

where

$$dP = \frac{1}{2}\rho v^2 \left(\frac{fL}{D_h}\right) \tag{9}$$

In the above equations f is the friction factor which is estimated using [29]. Additionally, the Nu can be estimated using the same reference which predicts the heat transfer coefficient h as $h = Nu\ k/H$. Knowledge of the temperature difference can be used to estimate the heat dissipation capacity of the microchannel heat sinks. The overall heat flux dissipation capacity is estimated to be 35 W and 56 W for the single microchannel and multiple microchannel cases, respectively. The heat dissipation capacities of microchannel cooling are thus comparable to those obtained from electrowetting-based discrete-droplet heat sinks operating at the same pumping power.

CONCLUSIONS

The heat removal capacity of droplets under electrowetting actuation is characterized via experiments and numerical analysis. Transient three-dimensional simulations are carried out to estimate the flow and temperature patterns associated with a droplet sliding on a plate or sandwiched between two plates. Several interesting, complex and non-intuitive fluid circulation patterns are observed; it is shown that these patterns significantly influence thermal transport and heat transfer coefficients. The complexity of the transient flow patterns underscores the need for careful analysis of the flow field and its effect on the heat removal capacity of droplet-based systems. Systematic experimentation is carried out to benchmark the models. The reduction in wall temperatures resulting from the motion of a relatively cold droplet is directly measured.

Further, the heat dissipation capacity of electrowetting-based systems is seen to be comparable to microchannel cooling systems operating at the same pumping power. Electrowetting-based systems offer significant other advantages over microchannel cooling such as the possibility for enhanced reconfigurable flow control, the absence of mechanical moving parts, noiselessness and ease of integration with existing microelectronics packaging frameworks. The present work thus forms the basis for further studies on the thermal performance of discrete droplet-based systems for cooling and phase change applications.

Acknowledgement

REFERENCES

[1] F. Mugele, and J. C. Baret, Electrowetting: from basics to applications, Journal of Physics: Condensed Matter 17 (2005) R705-R774.

[2] H. –S. Chuang, A. Kumar, and S. T. Wereley, Open optoelectrowetting droplet actuation, Applied Physics Letters 93 (2008) 064104.

[3] V. K. Pamula and K. Chakrabarty, Cooling of integrated circuits using droplet-based microfluidics, Proc. ACM Great Lakes Symposium on VLSI, 2003, pp. 84-87.

[4] P. Paik, V. K. Pamula and K. Chakrabarty, Adaptive hot-spot cooling of integrated circuits using digital microfluidics, Proceedings of IMECE, IMECE2005-81081, Florida (USA), 2005.

[5] K. Mohseni, Effective cooling of integrated circuits using liquid alloy electrowetting, Semiconductor Thermal Measurement and Management Symposium, 2005, pp. 20-25.

[6] L.H. J. Wachters, L. Smulders, J. R. Vermeulen, and H. C. Kleiweg, The heat transfer from a hot wall to impinging mist droplets in the spheroidal state, Chemical Engineering Science 21 (1996)1231–1238.

[7] S. Zhang and G. Gogos, Film evaporation of a spherical droplet over a hot surface – fluid-mechanics and heat mass-transfer analysis, Journal of Fluid Mechanics 222 (1991) 543–563.

[8] L.H.J. Wachters and N.A. Westerling, The heat transfer from a hot wall to impinging water drops in the spheroidal state, Chemical Engineering Science 21 (1996) 1047–1056.

[9] J.D.Bernardin, I. Mudawar, C. B. Walsh, and E. I. Franses, Contact angle temperature dependence for water droplets on practical aluminum surfaces, International Journal of Heat Mass Transfer 40 (5) (1997) 1017–1033.

[10] H. Fujimoto and N. Hatta, Deformation and rebounding processes of a water droplet impinging on a flat surface above Leidenfrost temperature, Journal of Fluid Engineering - Transactions. ASME 118 (1) (1996) 142–149.

[11] Z. Zhao, D. Poulikakos, and J. Fukai, Heat transfer and fluid dynamics during the collision of a liquid droplet on a substrate-I. Modeling, International Journal of Heat Mass Transfer 39 (13) (1996) 2771–2789.

[12] G. Strotos, M. Gavaises, A. Theodorakakos, and G. Bergeles, Numerical investigation of the cooling effectiveness of a droplet impinging on a heated surface, International Journal of Heat and Mass Transfer 51 (2008) 4728–4742.

[13] M. Trela, An approximate calculation of heat transfer during flow of an air-water mist along a heated flat plate, International Journal of Heat and Mass Transfer 24 (1981) 749-755.

[14] N. Kumari, V. Bahadur, M. Hodes, T. Salamon, P. Kolodner, A. Lyons, and S. V. Garimella, Analysis of evaporative mist flow for enhanced convective heat transfer, Internation Journal of Heat and Mass Transfer doi:10.1016/j.ijheatmasstransfer.2010.02.027.

[15] S. Chandra, M. diMarzo, Y. M. Qiao, and P. Tartarini, Effect of liquid-solid contact angle on droplet evaporation, Fire Safety Journal 27 (2) (1996) 141-158.

[16] O. E. Ruiz and W. Z. Black, Evaporation of water dropletsplaced on a heated horizontal surface, Journal of Heat Transfer 124 (5) (2002) 854-863.

[17] J. Fukai, M. Etou, F. Asanoma, and O. Miyatake, Dynamic contact angles of water droplets sliding on inclined hot surfaces. Journal of Chemical Engineering of Japan 33 (1) (2000) 177-179.

[18] L. Tarozzi, A. Muscio, and P. Tartarini, Experimental tests of dropwise cooling on infrared-transparent media, Experimental Thermal and Fluid Science 31 (2007) 857–865.

[19] P. Paik, V. M. Pamula, and K. Chakrabarty, Thermal effects on droplet transport in digital microfluidics with applications to chip cooling, Thermomechanical Phenomena in Electronic Systems -Proceedings of the Intersociety Conference 1 (2004) 649-654.

[20] H. Oprins, C. C. S. Nicole, J. C. Baret, G. Van der Veken, C. Lasance, and M. Baelmans, On-chip liquid cooling with integrated pump technology, Semiconductor Thermal Measurement and Management Symposium, 2005, pp. 347-353.

[21] H. Oprins, J. Danneels, B. Van Ham, B. Vandevelde, and M. Baelmans, Convection heat transfer in electrostatic actuated liquid droplets for electronics cooling, Microelectronics Journal 39 (2008) 966-974.

[22] E. Baird and K. Mohseni, Digitized heat transfer: A new paradigm for thermal management of compact micro systems, IEEE Transactions on Components and Packaging Technologies 31 (2008) 143-151.

[23] V. Bahadur and S. V. Garimella, Electrowetting-based control of droplet transitions and morphology on artificially microstructured surfaces, Langmuir 24 (2008) 8338-8345.

[24] V. Bahadur and S. V. Garimella, Energy minimization-based analysis of electrowetting for microelectronics cooling applications, Microelectronics Journal 39 (7) (2008) 957-965.

[25] NASA Jet Propulsion Laboratory Web Site, URL: http://masterweb.jpl.nasa.gov/reference/paints. htm.

[26] X. Zhu, H. Wang, Q. Liao, Y. D. Ding, and Y. B. Gu, Experiments and analysis on self-motion behaviors of liquid droplets on gradient surfaces, Experimental Thermal and Fluid Science 33 (2009) 947-954.

[27] FLUENT 6 User's Guide, Lebanon, NH, Fluent Inc., 2000.

[28] A. K. Das and P. K. Das, Simulation of drop movement over an inclined surface using smoothed particle hydrodynamics, Langmuir 25 (19) 2009 11459-11466.

[29] D. Liu and S. V. Garimella, Analysis and optimization of the thermal performance of microchannel heat sinks, International Journal of Numerical Methods for Heat and Fluid Flow 15 (2005), 7-26.

[30] N. Kumari, V. Bahadur and S. V. Garimella, Electrical actuation of electrically conducting and insulating droplets using ac and dc voltages, Journal of Micromechanics and Microengineering 18 (2008) 105015.

Table 1. Volume and terminal velocities of droplets.

Liquid	Volume (μl)	Velocity (cm/s)/ Tilt angle
Ethylene glycol	5	2.85/30°, 3.95/45° and 9/60°
	6.5	4.66/30°, 6.36/45° and 10.71/60°
Water	5	9/30°
	6.5	12.55/30°

Table 2. Comparison of heat dissipation capacity of droplet-based systems.

Droplet volume (μL)	Droplet radius (mm)	Plate spacing (mm)	Spacing between droplets (mm)	Number of droplets on 12×12 mm^2 area	% area covered by droplets	Heat transfer coefficient / heat flux (single droplet)	Average heat flux (W/cm^2)
5	1.78	0.5	0.1	3×3	62.5	7890 / 46	29
1	0.79	0.5	0.1	7×7	68.1	10190 / 59	40
1	1.78	0.1	0.1	3×3	62.5	3880 / 23	14

(a)

(b)
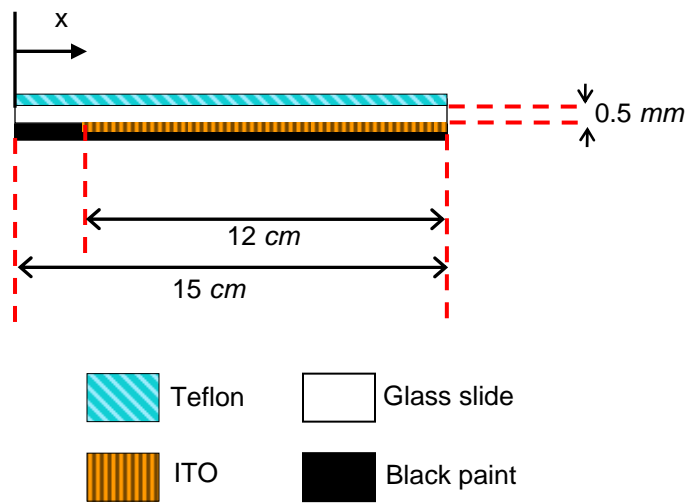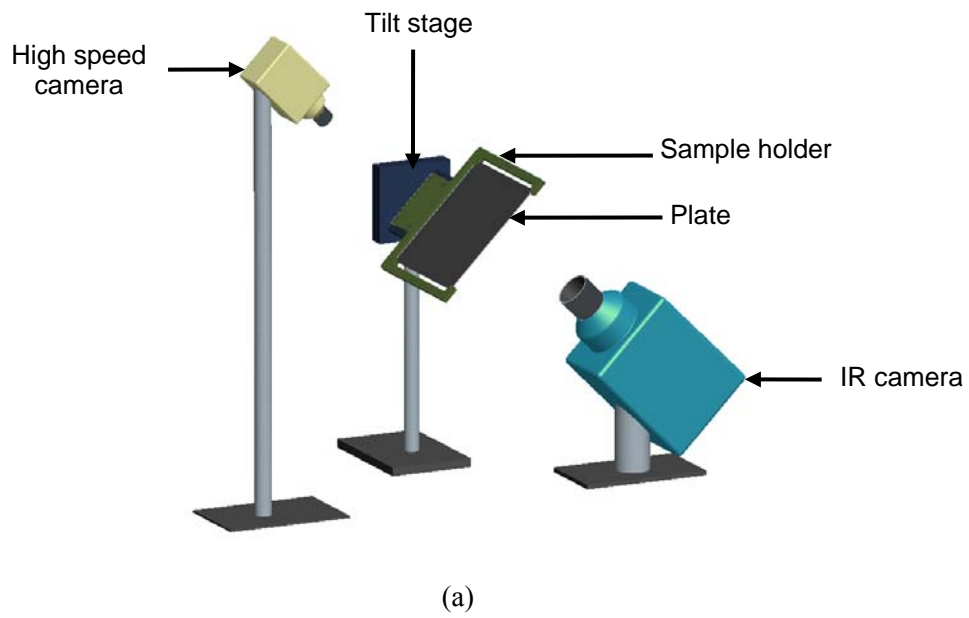
Figure 1. (a) Schematic diagram of the experimental setup for measuring droplet velocity and heat dissipation capacity, and (b) details of the plate cross section.

(a)

Droplet footprint
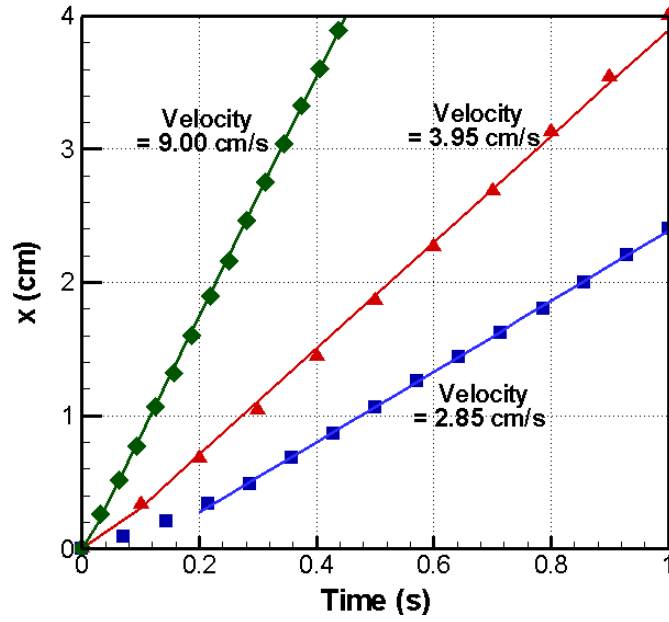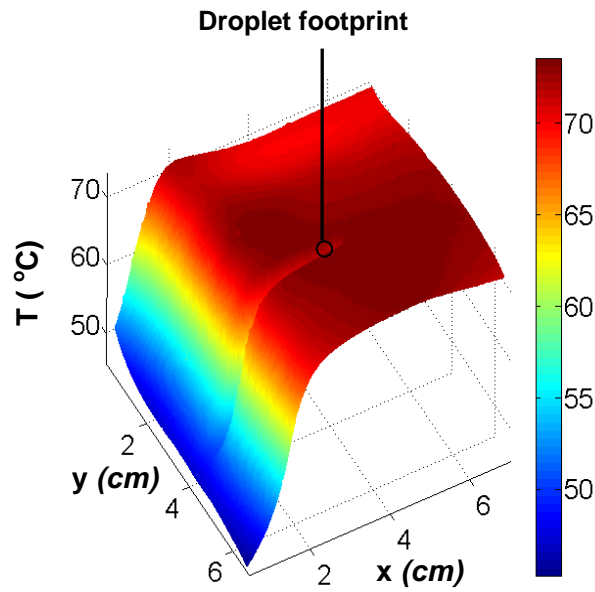
(b)

Figure 2. Experimental data for a 5 *μl* EG droplet: (a) transient droplet positions at different angles of inclination, and (b) temperature contours on the lower surface of the heated plate with the droplet moving at 3.95 *cm/s* on the upper surface.
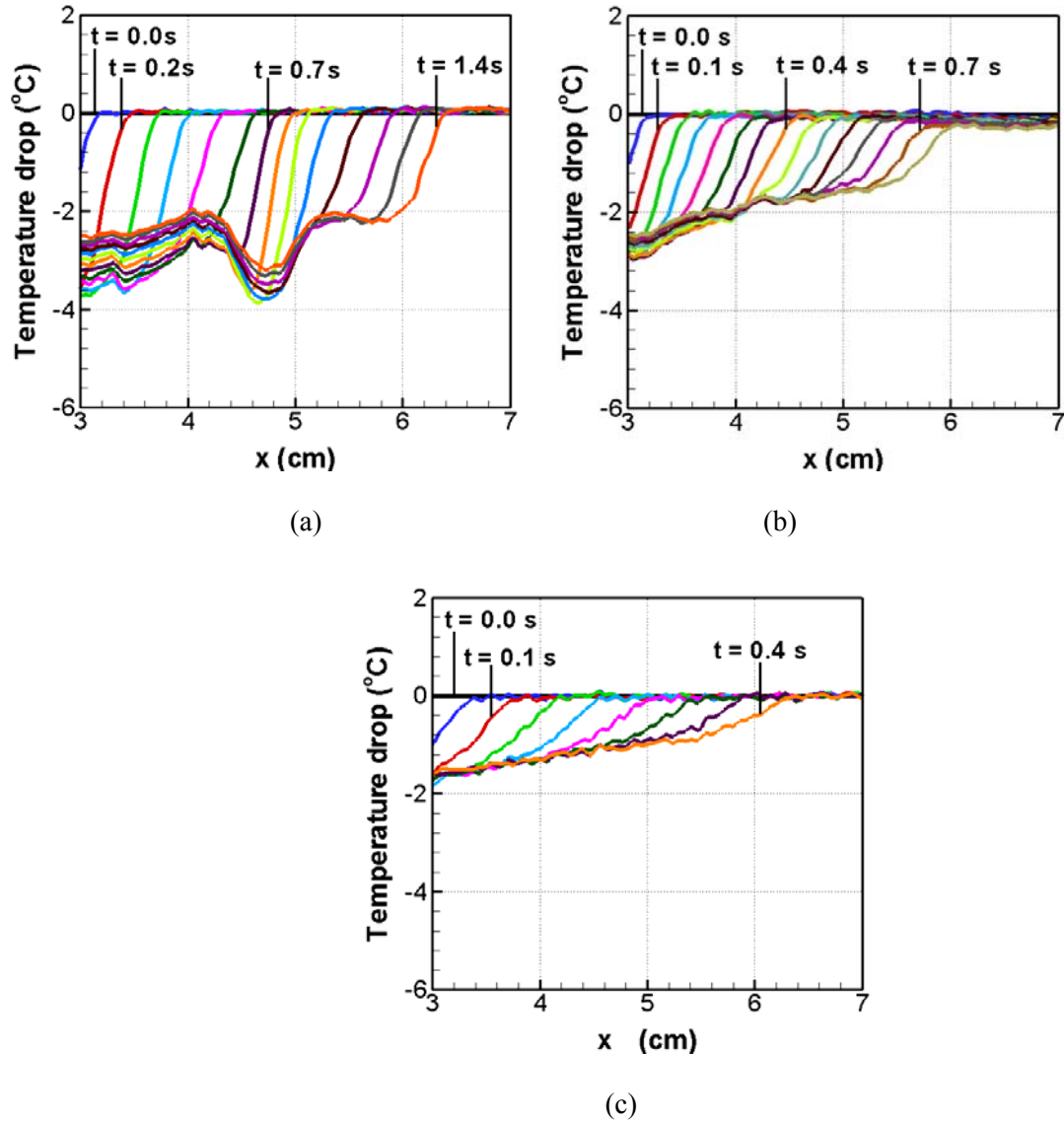
Figure 3. Experimentally measured temperature decrease along the centerline of the lower surface for a 5 *μl* EG droplet: (a) V = 2.85 *cm/s* (droplet center at 2.56 *cm* at t = 0, after which it moves by 0.167 *cm* every 0.05 *s*), (b) V= 3.95 *cm/s* (droplet center at 2.67 *cm* at t = 0, after which it moves by 0.188 *cm* every 0.05 *s*), and (c) V = 9 *cm/s* (droplet center at 3.35 *cm* at t = 0, after which it moves by 0.45 *cm* every 0.05 *s*).
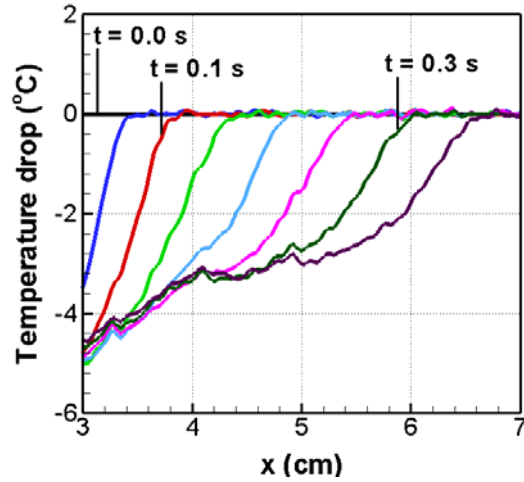
(a)
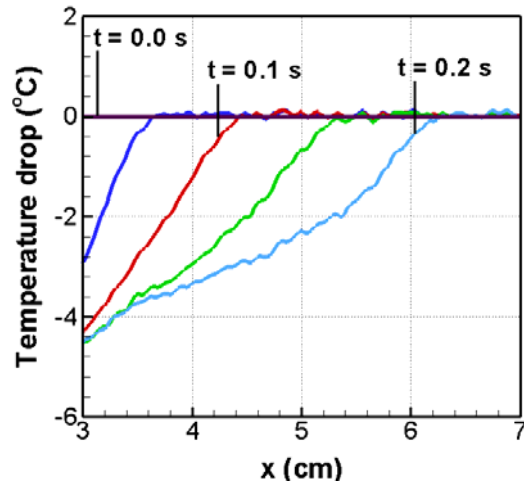
(b)

Figure 4. Experimentally measured temperature decrease along the centerline of the lower surface using water droplets (a) 5 *μl* droplets moving at 9 *cm/s* (droplet center at 2.76 *cm* at t = 0, after which it moves by 0.45 *cm* every 0.05 *s*), and (b) 6.5 *μl* droplets moving at 12.6 *cm/s* (droplet center at 3.02 *cm* at t = 0, after which it moves by 0.328 *cm* every 0.05 *s*)
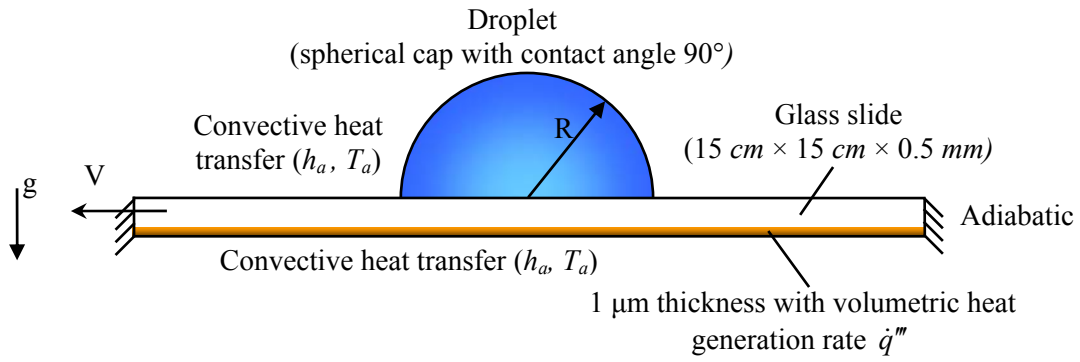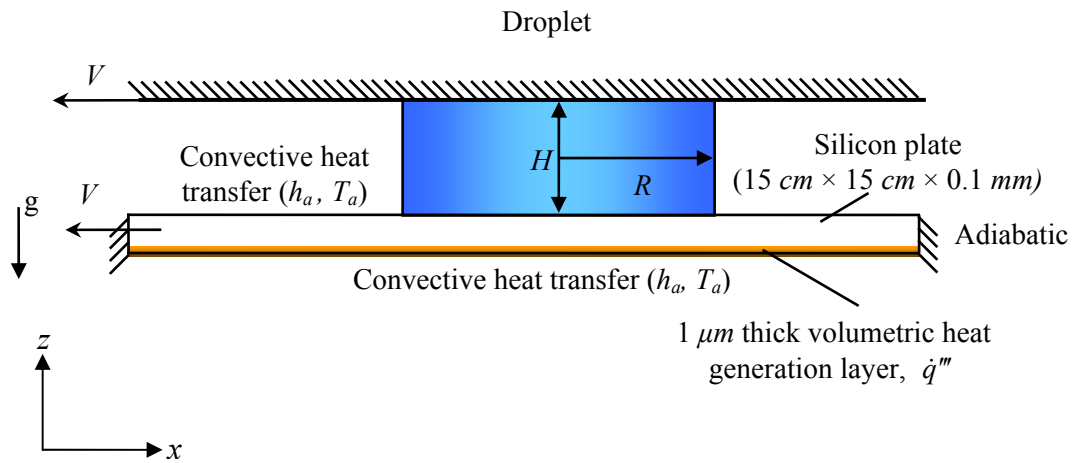
Figure 5 . Computational domain for droplet motion (a) on a heated plate, and (b) between two plates.
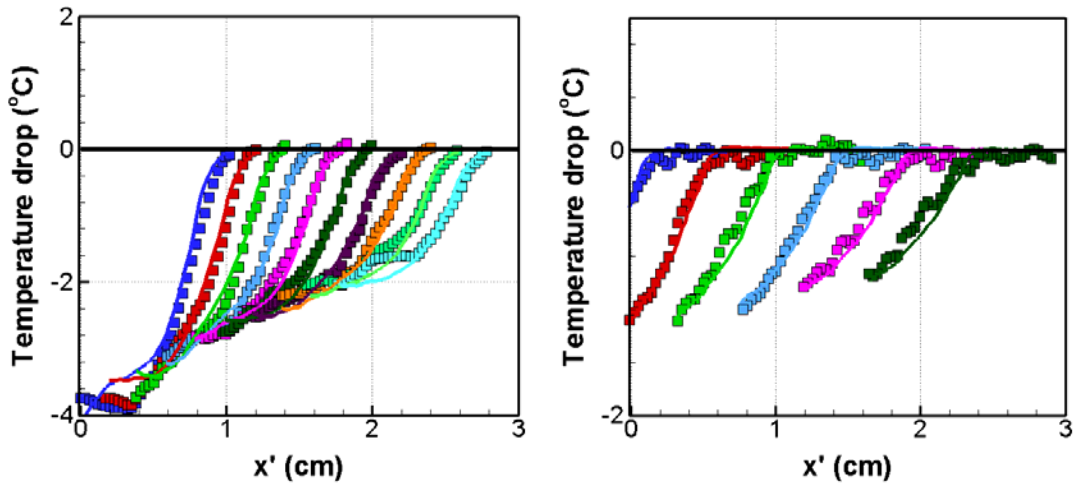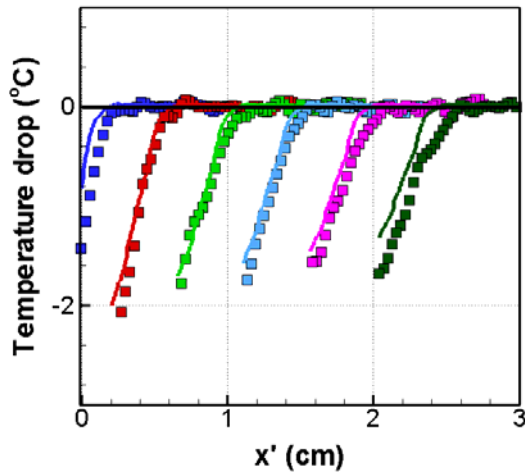
Figure 6. Comparison of the experimental and numerical temperature profiles for an ethylene glycol droplet moving on a heated plate at (a) 3.95 *cm/s* and (b) 9 *cm/s*, and (c) for a water droplet moving at *9 cm/s*. The droplet center for the first profile is at *x' =* 0.5 *cm* after which it moves 0.188 *cm* in (a), and 0.45 *cm* in (b) and (c) for each subsequent profile (symbols – experimental results, solid lines – numerical results).

(a) *y = 0 mm*   (b) *y = 0.4 mm*

(c) *z = 0.05 mm*   (d) *z = 0.2 mm*   (e) *z = 0.4 mm*

(f) *z = 0.5 mm*   (g) *z = 0.6 mm*   (h) *z = 0.7 mm*
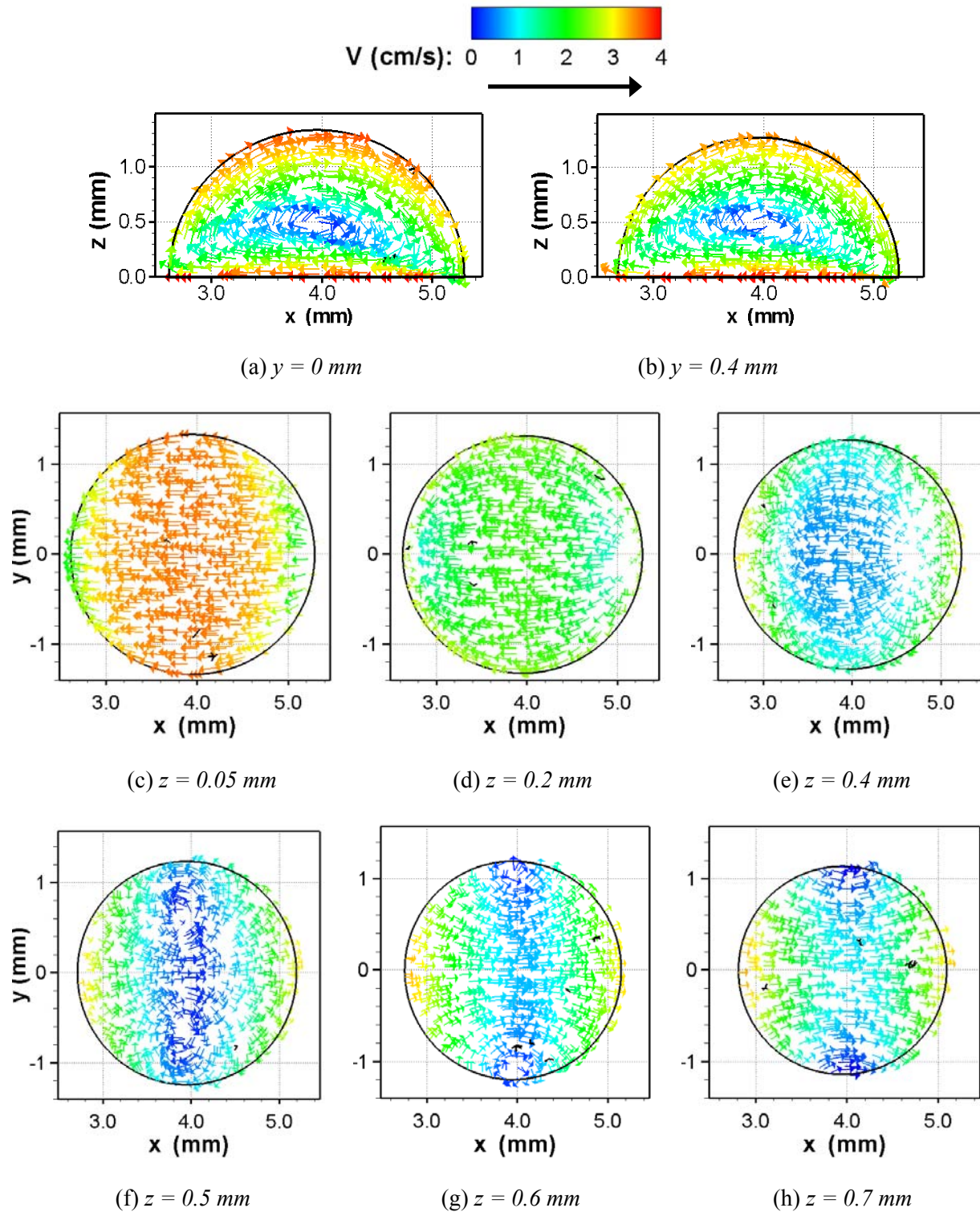
Figure 7. Velocity vectors for fully developed flow in a 5 *µL* ethylene glycol droplet moving at a velocity of 3.95 *cm/s* at 0.1 *s* on (a)-(b) *xz* planes (*y* = 0 *mm* and *y* = 0.4 *mm*), and (c)-(h) *xy* planes (*z* = 0.05, 0.2, 0.4, 0.5, 0.6 and 0.7 *mm*).
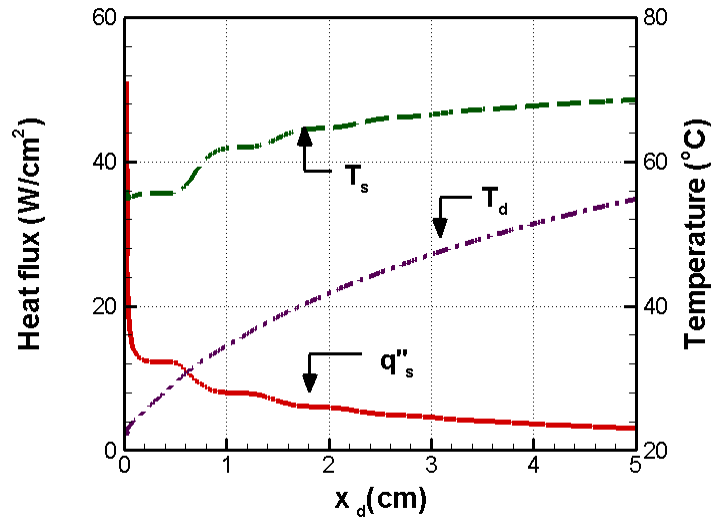
(a)
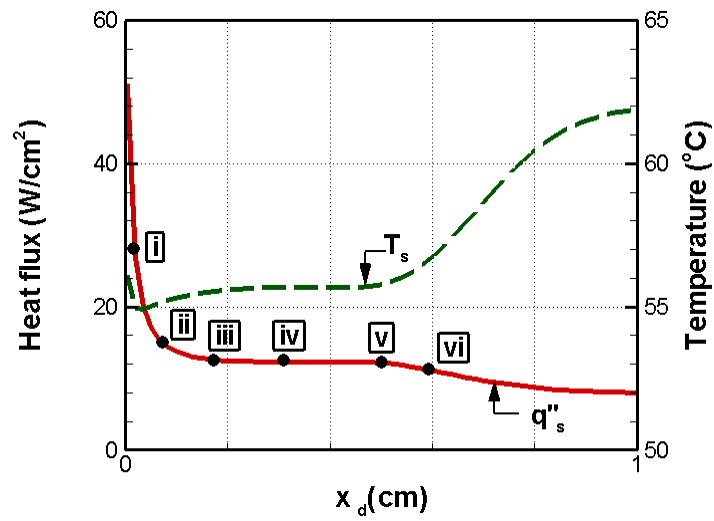
(b)

Figure 8. (a) Average heat flux q_s'', average droplet-plate interface temperature T_s and mean droplet temperature T_d as a function of droplet center location x_d for a 5 μL ethylene glycol droplet moving at 3.95 *cm/s*, and (b) a zoomed plot for $0 < x_d < 1$ cm.
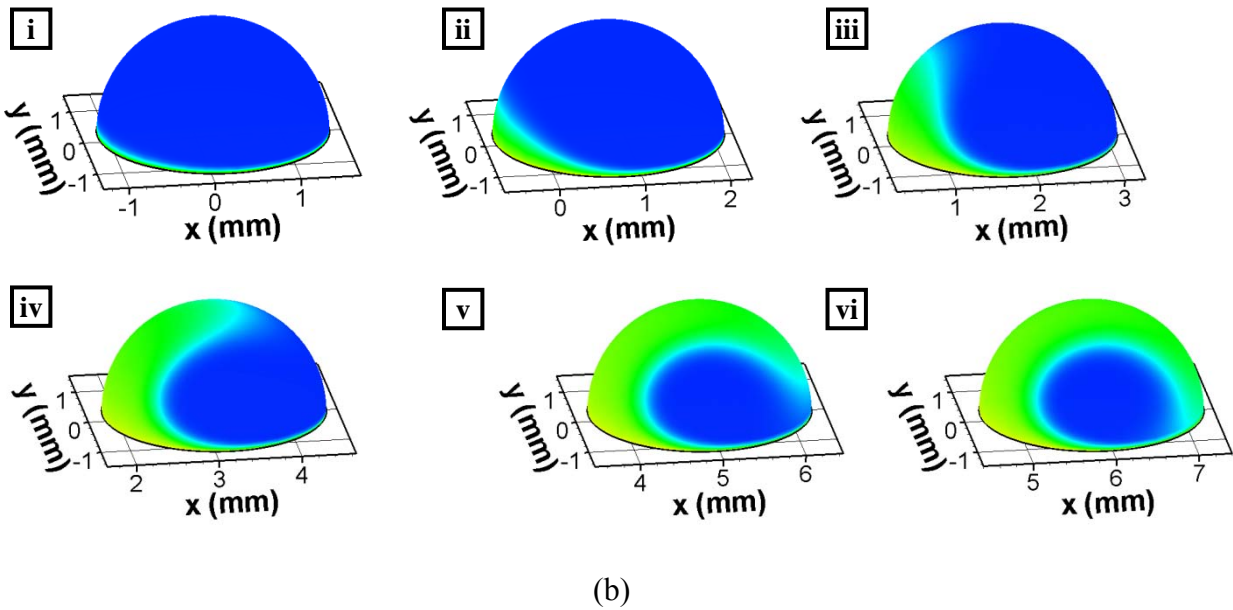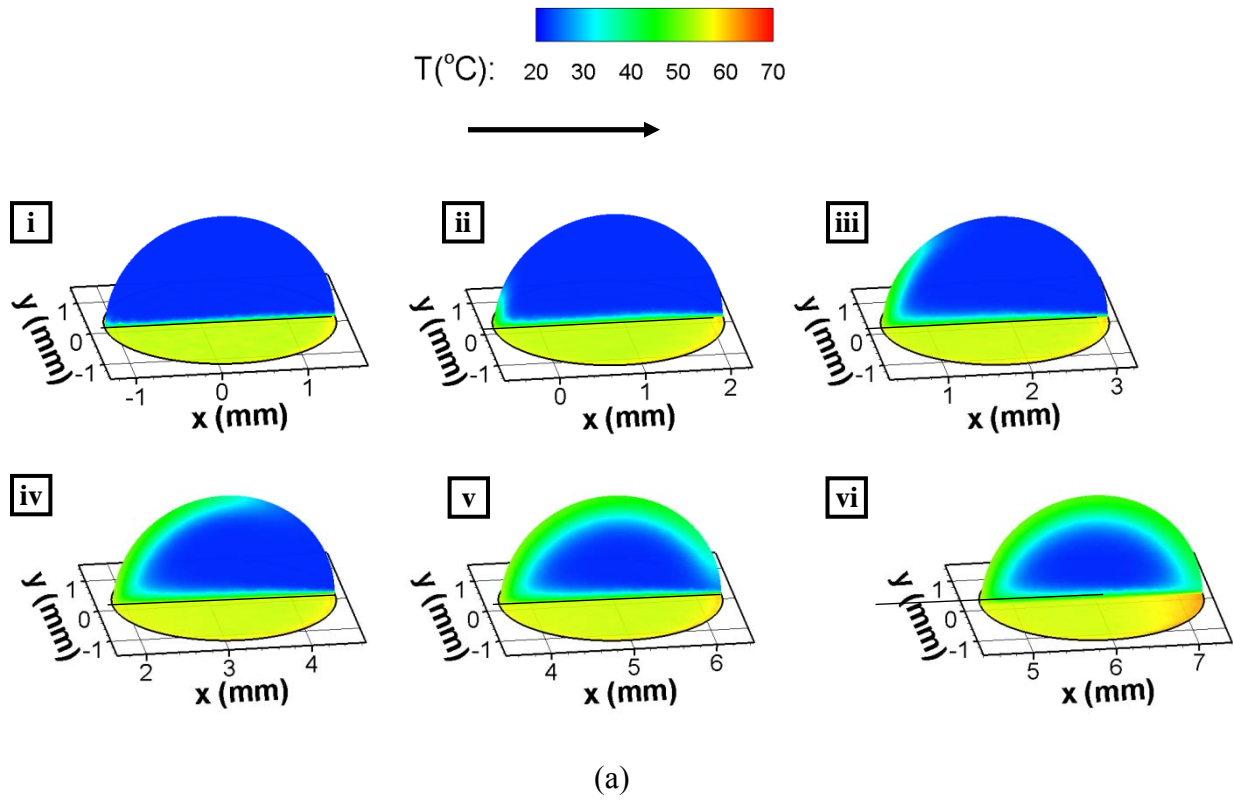
Figure 9. Temperature profile due to the motion of a 5 *µL* ethylene glycol droplet moving at 3.95 *cm/s* on (a) *xz* plane at *y* = 0 *mm* and droplet-plate interface, and (b) droplet-air interface.
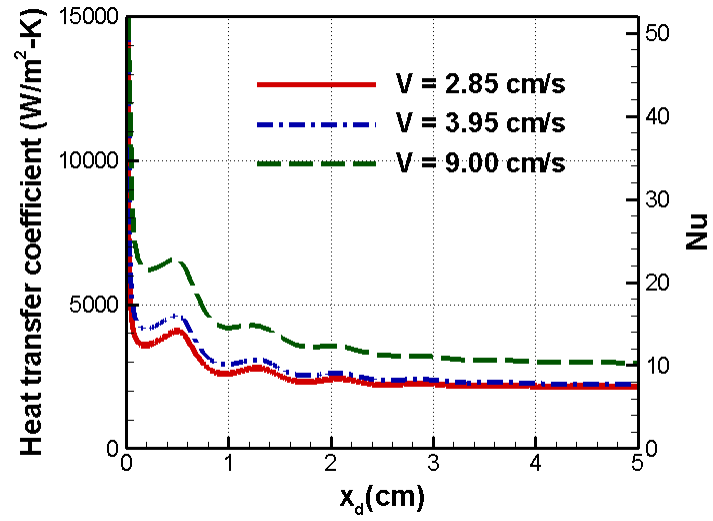
(a)
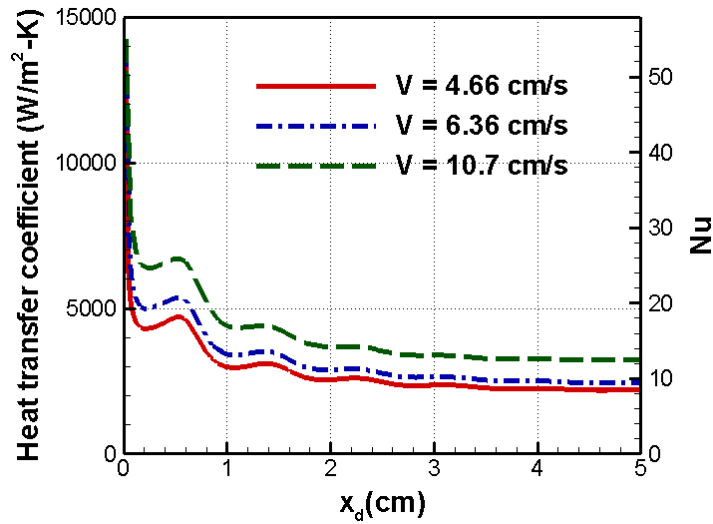
(b)

Figure 10. Variation of heat transfer coefficient and Nusselt number as a function of droplet position x_d for a (a) 5 μL, and (b) 6.5 μL ethylene glycol droplet moving with different velocities.
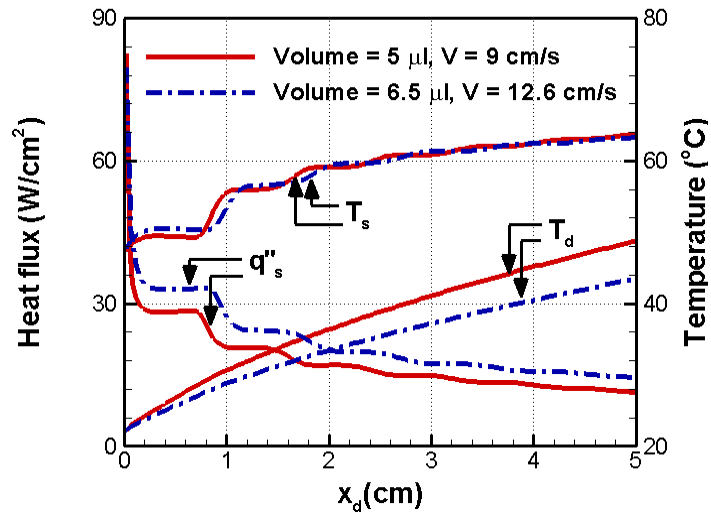
(a)
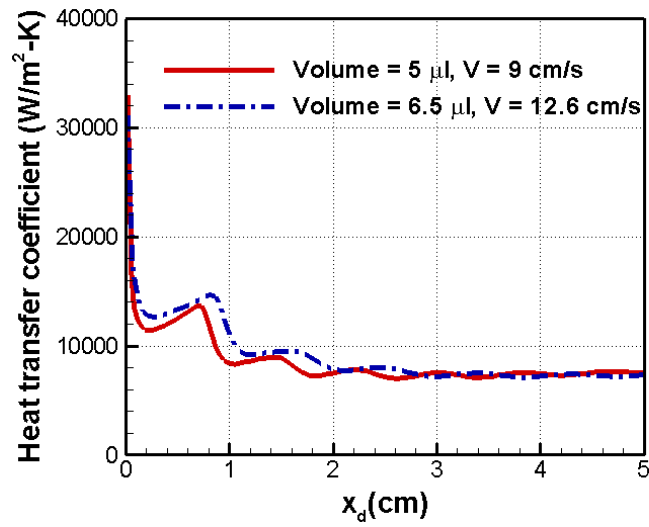
(b)

Figure 11. Heat transfer parameters during the motion of water droplets of different volume moving at different velocities: (a) $q_s^{''}$, T_s and T_d, and (b) heat transfer coefficient.

(a) Leading edge at *y* = 0 *mm* (b) Trailing edge at *y* = 0 *mm*

(c) *z* = 0.0 *mm* (d) *z* = 0.1 *mm* (e) *z* = 0.2 *mm*

(f) Velocity profile (v_x and v_z) at *y* = 0 *mm*
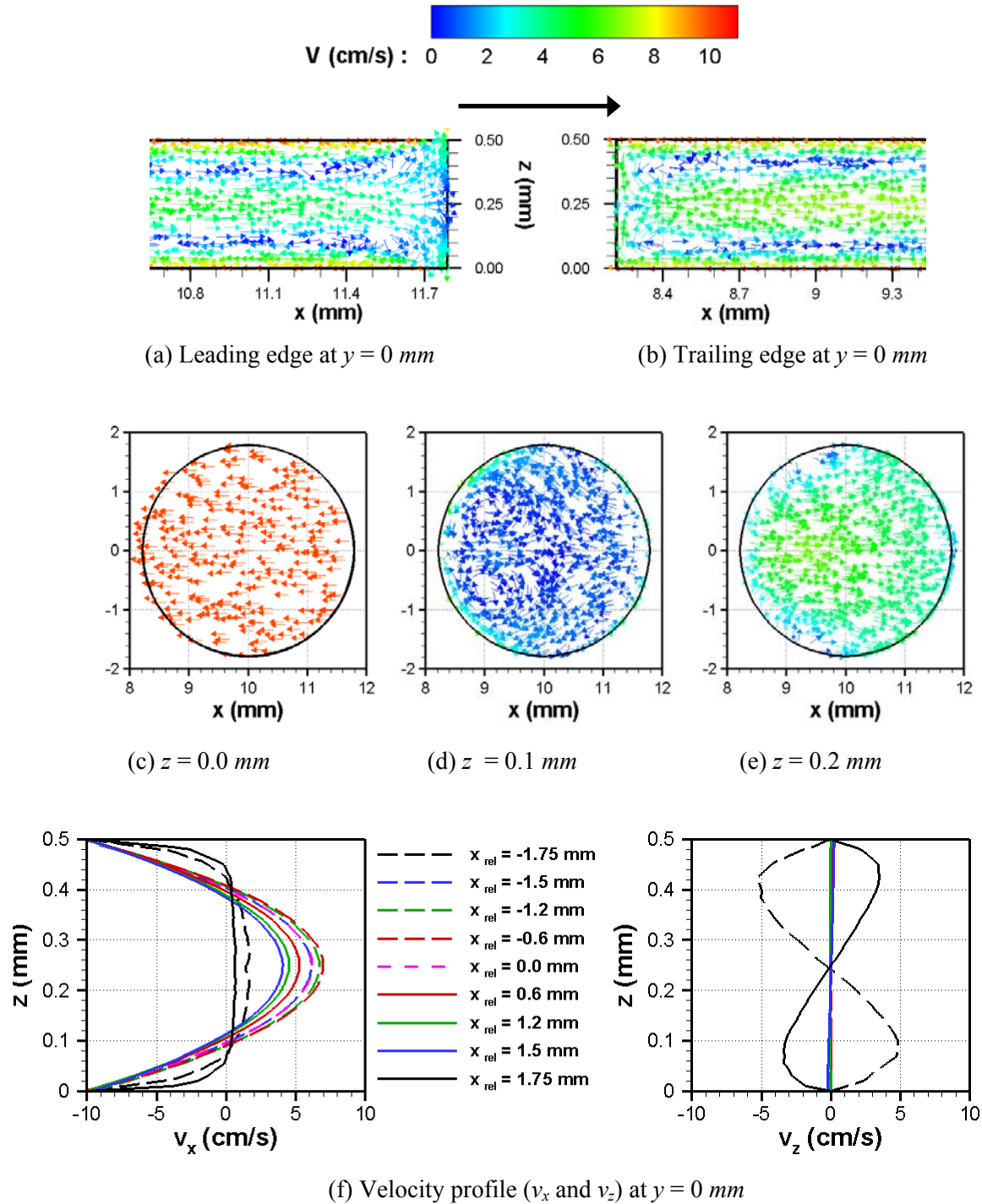
Figure 12. Velocity vectors (colored with velocity magnitude) at (a) leading edge, and (b) trailing edge of the droplet at *xz* plane, *xy* planes of droplet at (c) z = 0.1 *mm*, (d) z = 0.2 *mm* and (e) z = 0.3 *mm*; and (f) Velocity profiles v_x and v_z at y = 0 *mm* at different axial distances. Droplet motion direction is shown by the top arrow (x_{rel} is measured with respect to the center of the droplet, *x* = 10 *mm*).
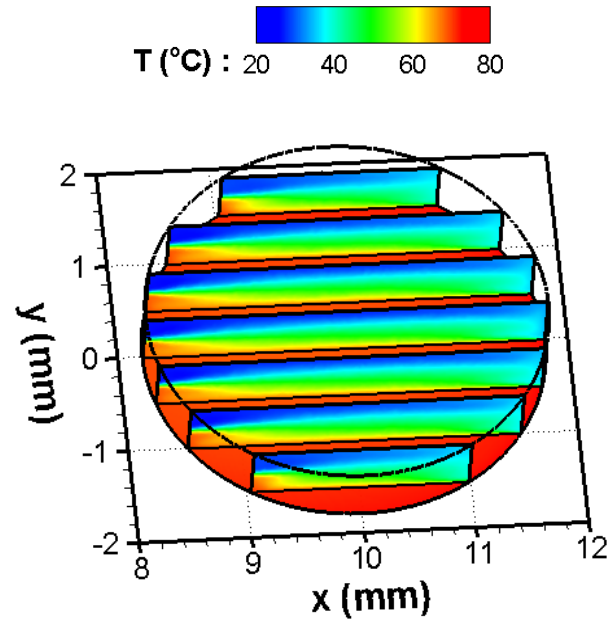
(a)
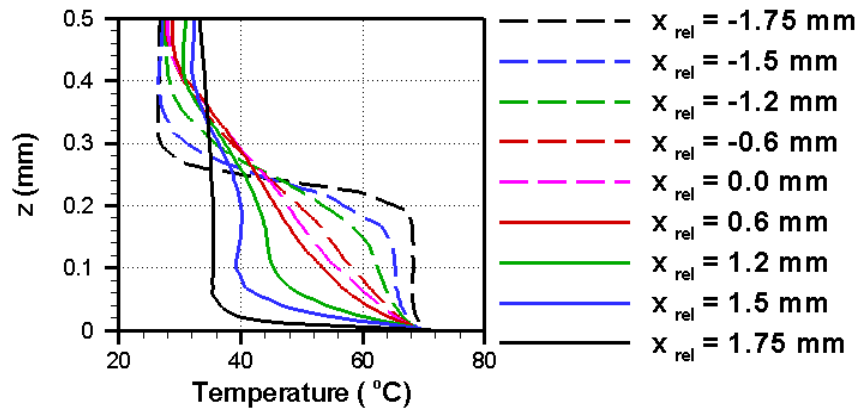
(b)

Figure 13. (a) Temperature contours plot at *xz* planes at *y* = 0, ± 0.5, ± 1.0, ± 1.5 *mm*, and (b) temperature profiles at the *y* = 0 plane at different axial distances. Note that x_{rel} is measured with respect to the center of the droplet, *x* = 10 *mm*.
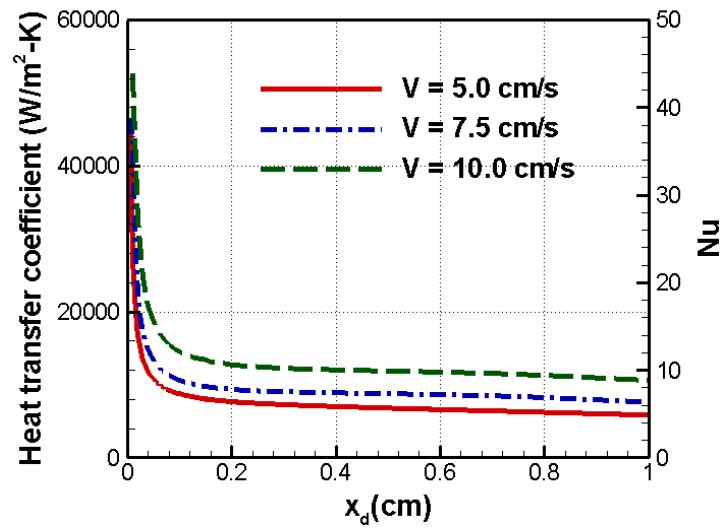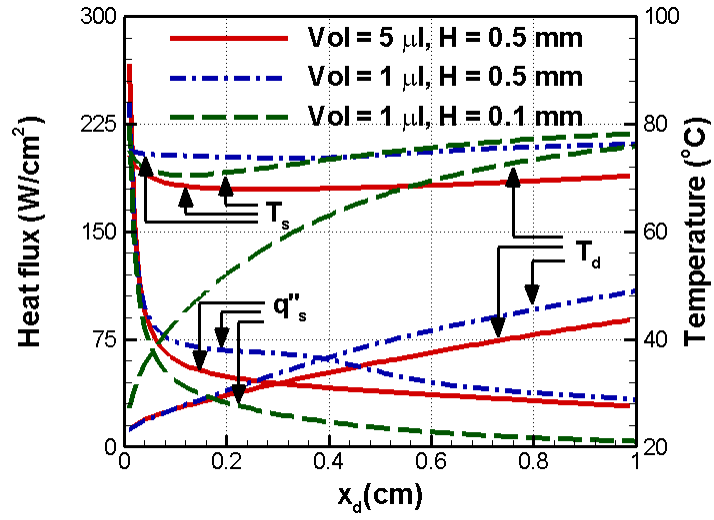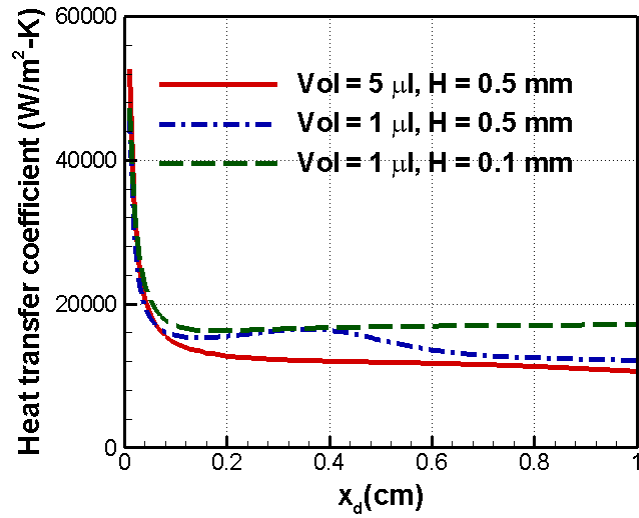
Figure 14. Heat transfer coefficient and Nusselt number as functions of the droplet center position x_d for water droplets moving with different velocities.

Figure 15. Heat transfer parameters associated with the motion of droplets of different volumes moving at 10 cm/s between two plates with different plate spacings: (a) $q_s^{''}$, T_s and T_d, and (b) the heat transfer coefficients.